

Simulating Damage and Permanent Strain in Composites under In-plane Fatigue Loading

W. Van Paepegem* and J. Degrieck

Ghent University, Dept. of Mechanical Construction and Production,
Sint-Pietersnieuwstraat 41, 9000 Gent, Belgium

Abstract

Fibre-reinforced composites are used in many fatigue-critical applications (wind turbine blades, aircraft components, leaf springs,...). Due to their heterogeneous and anisotropic nature, their fatigue behaviour is rather complex and several damage mechanisms can develop during fatigue life. This paper presents a damage mechanics based fatigue model for fibre-reinforced plastics, where both stiffness degradation and (possible) accumulation of permanent strain are simulated from the first loading cycle up till final failure. The model has been validated for cantilever bending fatigue tests of plain woven glass/epoxy composite. Although the damage growth rate varies along the specimen length, the finite element simulations with the damage model are able to account for decreasing (bending) stiffness and permanent strain.

Keywords: composite, fatigue, damage mechanics, finite element analysis, stiffness.

1 Introduction

The existing fatigue models for fibre-reinforced composites can generally be classified into [1]: (i) fatigue life models (S-N curves), (ii) damage accumulation models ('mechanistic models'), and (iii) phenomenological residual stiffness/strength models. The scope of most models is limited to one-dimensional fatigue loading, although some models have been applied to multi-axial fatigue loading.

In the category of fatigue life models, the multi-axial loading problem is often handled by introducing a static failure criterion (e.g. Tsai-Wu, Tsai-Hill) and replacing the static strengths with the fatigue strengths in the criterion. This approach was followed by Lawrence Wu [2], Jen and Lee [3,4] and Philippidis and Vassilopoulos [5]. The drawback of this approach is that the fatigue strengths must be determined experimentally for different stress amplitudes, stress ratios and bi-axiality ratios. This requires a large experimental input of S-N curves which represent directly the perceived nature of fatigue in terms of experimental results, but give no indication of the mechanisms of fatigue damage, of the presence or behaviour of cracks, or of changes in the characteristics of the material as a consequence of the fatigue process.

Well-known mechanistic models for multi-axial fatigue loading are the continuum damage models by Talreja [6,7], Allen et al. [8,9] and Sedrakian et al. [10,11]. Recently, Shokrieh and Lessard [12,13] proposed a so-called 'generalized residual material property degradation

* Corresponding author (Fax: +32-(0)9-264.35.87, E-mail: Wim.VanPaepegem@UGent.be).

model' for unidirectionally reinforced laminates which uses Hashin-type fatigue failure criteria to determine the damage mode and consequently reduces the corresponding elastic properties.

In this paper, the phenomenological residual stiffness approach is adopted to simulate stiffness degradation, stress redistribution and permanent strain in fibre-reinforced polymers under generalized in-plane loading. The presence of each of these phenomena was clearly indicated by the experimental results which were obtained from displacement-controlled bending fatigue tests on plain woven glass/epoxy composites.

2 Experimental Setup and Material

2.1 Experimental Setup

Figure 1 shows the experimental setup for displacement-controlled cantilever bending fatigue tests. The shaft (point D in Figure 1) bears a mechanism with crank and connecting rod, which imposes an alternating displacement on the hinge (point C in Figure 1) that connects the connecting rod with the moving clamp of the composite specimen.

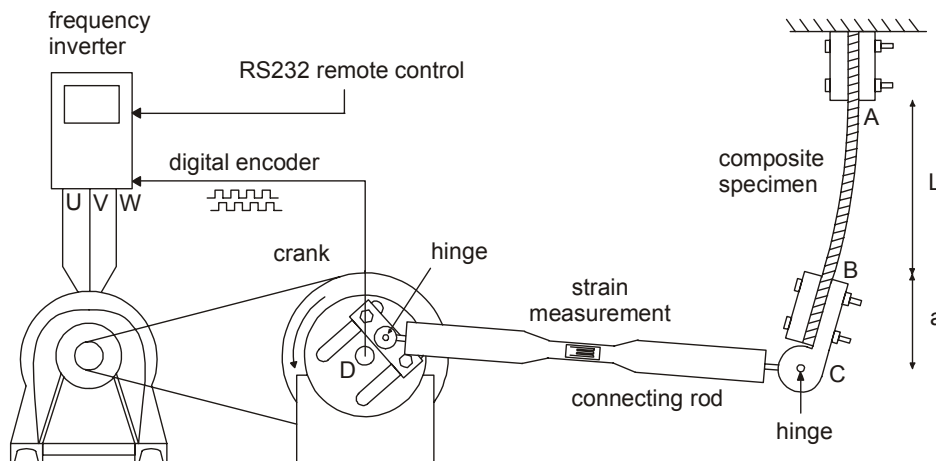


Figure 1: Schematic drawing of the experimental setup.

At the upper end the specimen is clamped (point A in Figure 1). Hence the sample is loaded as a composite cantilever beam. The force necessary to bend the specimen, is measured by means of a strain-gauge bridge on the connecting rod. The testing frequency is 2.2 Hz.

The amplitude u_{\max} of the prescribed displacement is defined as the orthogonal distance between the centre of the hinge (point C in Figure 1) and the vertical line passing through the midplane of the undeformed specimen (see Figure 2). The amplitude u_{\max} can be adjusted by changing the position of the crank, and its sign is positive in the direction indicated in Figure 2.

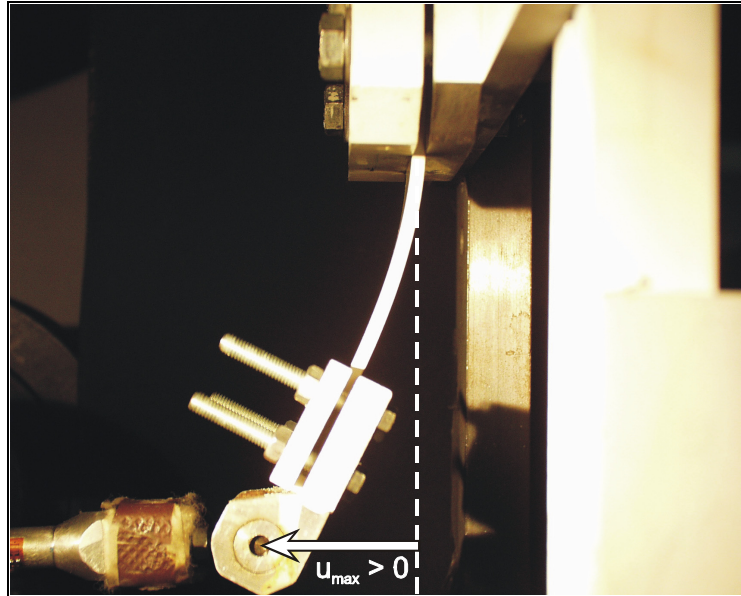


Figure 2: Definition of the amplitude u_{\max} of the prescribed displacement.

2.2 Material

The selected material was a plain woven glass fabric/epoxy composite, because of its widespread application in aerospace industry [14]. The use of fabrics is particularly attractive due to their better drapability for complex geometries, reduced manufacturing costs and increased resistance to (impact) damage [15]. Further, the transparency of the laminate facilitates visual inspection for damage.

For the first stacking sequence, the warp direction of all eight layers was aligned with the loading direction (denoted as $[\#0^\circ]_8$, where ‘0°’ means that the warp direction of each of the eight layers has been aligned with the loading direction and where the hash mark ‘#’ refers to the fabric reinforcement type). For the second stacking sequence, the angle between the warp direction of all layers and the loading direction was 45° (denoted as $[\#45^\circ]_8$). The two stacking sequences are supposed to represent two fundamentally different stress states. The bending of the $[\#0^\circ]_8$ stacking sequence results in a quasi one-dimensional loading of the laminate, with large stresses along the longitudinal fibre direction. In the $[\#45^\circ]_8$ stacking sequence, the load is sustained by a combined state of normal stresses in the two fibre directions of the fabric, and shear stresses.

The material was fabricated by resin transfer moulding, and a full characterization of the composite material was performed. All specimens had a fibre volume fraction of 0.48 and a thickness of 2.72 mm. They were cut to dimensions of 145 mm long by 30 mm wide.

3 Experimental Observations

Figure 3 shows the force-cycle history for a $[\#0^\circ]_8$ and $[\#45^\circ]_8$ specimen, subjected to single-sided bending with $u_{\max} = 34.4$ mm. The abscissa contains the number of cycles; the ordinate axis shows the force [Newton], which is measured by the strain gauge bridge on the connecting rod (Figure 1) during the fatigue tests.

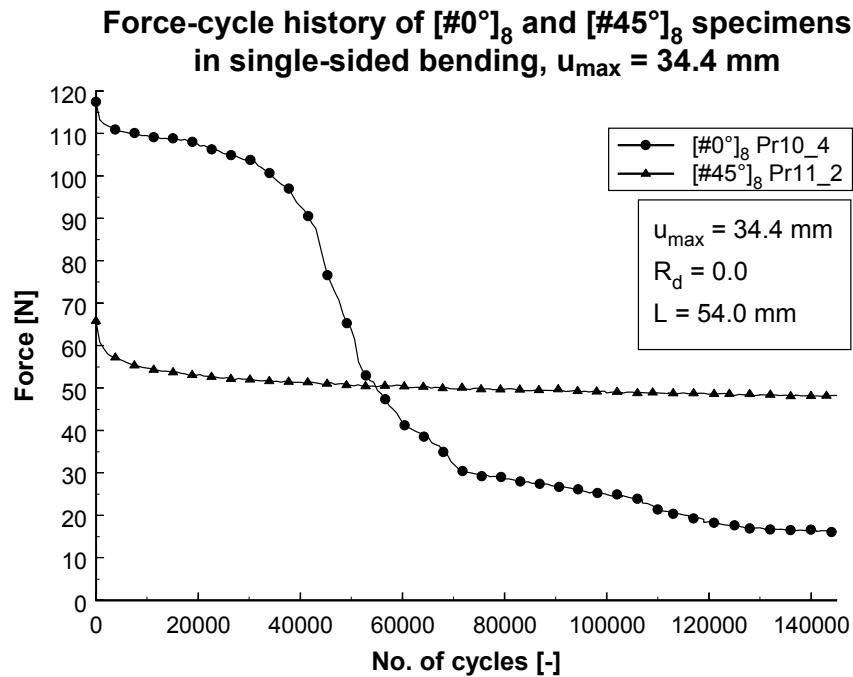


Figure 3: Force-cycle histories for $[\#0^\circ]_8$ and $[\#45^\circ]_8$ specimens (single-sided bending, $u_{\max} = 34.4$ mm).

The $[\#0^\circ]_8$ specimens degrade gradually in the early loading cycles, but their stiffness is reduced significantly after about 40,000 cycles. The initial force on the $[\#45^\circ]_8$ specimen is smaller, because its stiffness is lower. However, after 50,000 cycles, its remaining stiffness has become larger than that of the $[\#0^\circ]_8$ specimen. Of course the ratio of the surface strain to the ultimate strain is different for the two specimen types. This can be easily demonstrated by a structural analysis of the laminate when a constant curvature κ_x is imposed. The Tsai-Wu failure criterion will reach its failure value much earlier for the $[\#0^\circ]_8$ specimen than for the $[\#45^\circ]_8$ specimen, because the stresses, resulting from the imposed curvature, are smaller for the $[\#45^\circ]_8$ specimen.

The evolution of the out-of-plane displacement profile for both stacking sequences can be quite different as well. The out-of-plane displacement profile of the $[\#0^\circ]_8$ specimens can change from a smoothly curved profile at the early loading stage to a straight line at failure. Indeed, Figure 4 shows the out-of-plane displacement profile for the $[\#0^\circ]_8$ specimen Pr10_3 at the first loading cycle (left) and at final failure (right) for $u_{\max} = 36.8$ mm. As can be seen from this Figure, the out-of-plane displacement profile can change drastically.

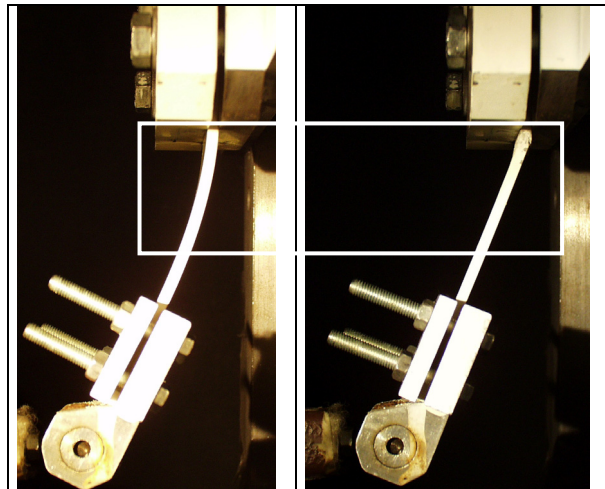


Figure 4: Out-of-plane displacement profile for $[\#0^\circ]_8$ specimen Pr10_3 at the first loading cycle (left) and at final failure (right) ($u_{\max} = 36.8$ mm).

Another aspect which should be paid attention to, is the accumulation of permanent strain for the $[\#45^\circ]_8$ specimens under large prescribed displacements. Indeed, when u_{\max} is large, a substantial permanent deformation did remain after removing the grips from the $[\#45^\circ]_8$ specimens, while this was not the case for the $[\#0^\circ]_8$ specimens.

Figure 5 shows the out-of-plane displacement profiles for the $[\#45^\circ]_8$ specimen Pr11_3 during fatigue life and after removing the lower clamp for $u_{\max} = 37.8$ mm. These out-of-plane displacement profiles have been recorded with the developed digital phase-shift shadow moiré technique [16]. As can be seen from the Figure, the permanent deformation is not at all negligible.

Figure 6 shows a picture of the $[\#45^\circ]_8$ specimens Pr06_3, Pr06_4 and Pr06_5, after having been subjected to a prescribed displacement u_{\max} of 38.9 mm for about 900000 loading cycles. The specimen at the right-hand side of the picture is an undamaged specimen for comparison purpose.

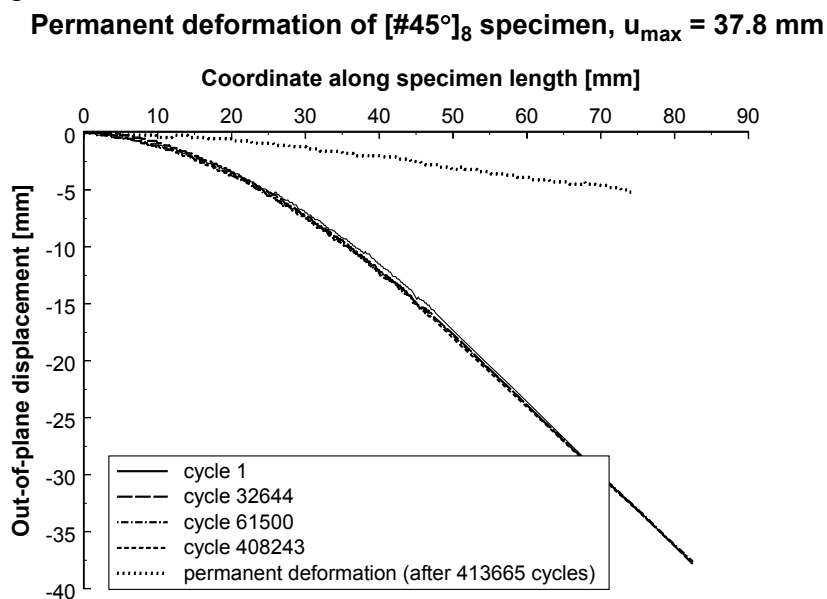


Figure 5: Out-of-plane displacement profiles of $[\#45^\circ]_8$ specimen Pr11_3 during fatigue life ($u_{\max} = 37.8$ mm).



Figure 6: Permanent deformation of $[\#45^\circ]_8$ specimens after removing the lower clamp.

In recent papers, the authors have proposed a one-dimensional model for simulation of the fatigue behaviour of the $[\#0^\circ]_8$ specimens [17-19]. Comparison of the experimental results of the $[\#0^\circ]_8$ and $[\#45^\circ]_8$ specimens shows here that a multi-dimensional model is necessary to simulate the fatigue behaviour of the $[\#45^\circ]_8$ specimens. Further, the $[\#0^\circ]_8$ specimens did not show any permanent deformation (only after failure, when fibres were broken), while the $[\#45^\circ]_8$ specimens clearly build up permanent strains. In the next paragraph, the outlines of the multi-dimensional fatigue damage model are presented.

4 Fatigue Damage Model

4.1 General Description

In order to simulate these experimentally observed phenomena, the model should be able to simulate: (i) stiffness degradation (decreasing bending force), (ii) stress redistribution (changing bending profiles), and (iii) accumulation of permanent strain.

To that purpose, a residual stiffness model was developed with three damage variables: D_{11} (damage in the \vec{e}_{11} direction), D_{22} (damage in the \vec{e}_{22} direction), and D_{12} (shear damage). These damage variables are directly related with the corresponding stress components σ_{11} (positive/negative), σ_{22} (positive/negative) and σ_{12} in the orthotropic directions of the

glass/epoxy composite. For each of the three damage variables, the growth rate per fatigue cycle N is defined by a differential equation $d(D_{ij})/dN$. To make a prediction of the moment of failure, the governing stresses σ_{11} , σ_{22} and σ_{12} in the corresponding differential equations have been replaced by the newly defined *fatigue failure indices* Σ_{11} , Σ_{22} en Σ_{12} . These failure indices are calculated from the Tsai-Wu static failure criterion, where the nominal stresses σ_{11} , σ_{22} , and σ_{12} are replaced by the effective stresses $\tilde{\sigma}_{11}$, $\tilde{\sigma}_{22}$ and $\tilde{\sigma}_{12}$ (defined as $\sigma_{ij}/(1-D_{ij})$). As such, there is a correlation with residual strength, and the moment of failure in the displacement-controlled bending fatigue tests can be predicted as well.

Finally, the permanent strains ε_{ii}^p ($i=1,2$) have been introduced. The growth rate $d(\varepsilon_{ii}^p)/dN$ is proportional with the elastic strain ε_{ii} and the growth rate $d(D_{12})/dN$.

4.2 Relevant Equations

Three relationships make up the complete modelling framework: (i) the damage-stiffness relationships, (ii) the fatigue damage evolution laws $d(D_{ij})/dN$, and (iii) the growth laws for the permanent strains ε_{ii}^p . These three relationships are discussed in the following paragraphs. A detailed justification of all equations is beyond the scope of this paper and has been the result of a larger research programme which can be found in Reference [20].

4.2.1 Damage-stiffness Relationships

It is first postulated that there is a distinct difference between the damage kinetics of intra-layer damage (matrix cracks, fibre/matrix debonding, fibre fracture,...) and inter-layer damage (delaminations). Moreover the responsible stress components are not the same. The in-plane stresses (σ_{11} , σ_{22} and σ_{12}) are affecting the intra-layer damage, while the out-of-plane stresses (σ_{13} , σ_{23} and σ_{33}) are causing inter-layer damage. Delaminations were not taken into account and the stacking sequence was chosen such that delaminations did not develop under the experimental loading conditions. Therefore free edge effects are excluded from the model. If only intra-layer damage is considered, it is postulated that there exist three damage variables D_{11} , D_{22} and D_{12} , which are defined through the relations:

$$\begin{Bmatrix} \sigma_{11} \\ \sigma_{22} \\ \sigma_{33} \\ \sigma_{23} \\ \sigma_{13} \\ \sigma_{12} \end{Bmatrix} = \begin{bmatrix} \sqrt{1-D_{11}} & 0 & 0 & 0 & 0 & 0 \\ 0 & \sqrt{1-D_{22}} & 0 & 0 & 0 & 0 \\ 0 & 0 & 1 & 0 & 0 & 0 \\ 0 & 0 & 0 & 1 & 0 & 0 \\ 0 & 0 & 0 & 0 & 1 & 0 \\ 0 & 0 & 0 & 0 & 0 & \sqrt{1-D_{12}} \end{bmatrix} \cdot \begin{Bmatrix} C_{11} & C_{12} & C_{13} & 0 & 0 & 0 \\ C_{12} & C_{22} & C_{23} & 0 & 0 & 0 \\ C_{13} & C_{23} & C_{33} & 0 & 0 & 0 \\ 0 & 0 & 0 & C_{44} & 0 & 0 \\ 0 & 0 & 0 & 0 & C_{55} & 0 \\ 0 & 0 & 0 & 0 & 0 & C_{66} \end{Bmatrix} \quad (1)$$

$$\begin{bmatrix} \sqrt{1-D_{11}} & 0 & 0 & 0 & 0 & 0 \\ 0 & \sqrt{1-D_{22}} & 0 & 0 & 0 & 0 \\ 0 & 0 & 1 & 0 & 0 & 0 \\ 0 & 0 & 0 & 1 & 0 & 0 \\ 0 & 0 & 0 & 0 & 1 & 0 \\ 0 & 0 & 0 & 0 & 0 & \sqrt{1-D_{12}} \end{bmatrix} \cdot \begin{Bmatrix} \varepsilon_{11} - \varepsilon_{11}^p \\ \varepsilon_{22} - \varepsilon_{22}^p \\ \varepsilon_{33} \\ 2\varepsilon_{23} \\ 2\varepsilon_{13} \\ 2\varepsilon_{12} \end{Bmatrix}$$

where $[C]$ is the initial orthotropic stiffness matrix of the composite material. The permanent strains ε_{11}^p and ε_{22}^p must account for the permanent deformation of the $[\#45^\circ]_8$ specimens (see Figure 5 and 6). Although this Equation represents a simplified approach, it is at least manageable in terms of number of damage variables and finite element implementation, because the symmetry of the stiffness matrix $[C]$ is guaranteed at any time during fatigue life.

A very important advantage of the formulation in Equation (1) is that the damage variables D_{11} , D_{22} and D_{12} are directly related with their respective stress components σ_{11} , σ_{22} and σ_{12} . As such, the damage growth rates dD_{11}/dN , dD_{22}/dN and dD_{12}/dN are driven by the respective stresses σ_{11} , σ_{22} and σ_{12} . Further, there is a very clear distinction between positive and negative stresses for each of the damage variables. Indeed, for each damage variable, the sign of the corresponding stress component dictates which damage growth rate equation should be used, the one for tension or the one for compression.

It could be argued that there is no direct coupling between the damage variables D_{11} , D_{22} and D_{12} . However, this only seems so, because in the next paragraph, it will be shown that the damage evolution laws dD_{11}/dN , dD_{22}/dN and dD_{12}/dN are coupled.

4.2.2 Fatigue Damage Evolution Laws

The final objective is the development of a set of damage growth rate equations of the form:

$$\frac{dD_{11}}{dN} = \begin{cases} f_1(\sigma_{ij}, D_{ij}) & \text{if } \sigma_{11} \geq 0 \\ f_2(\sigma_{ij}, D_{ij}) & \text{if } \sigma_{11} < 0 \end{cases}$$

$$\frac{dD_{22}}{dN} = \begin{cases} g_1(\sigma_{ij}, D_{ij}) & \text{if } \sigma_{22} \geq 0 \\ g_2(\sigma_{ij}, D_{ij}) & \text{if } \sigma_{22} < 0 \end{cases} \quad (2)$$

$$\frac{dD_{12}}{dN} = h(\sigma_{ij}, D_{ij})$$

Each damage growth rate equation should depend on the multi-axial in-plane stress state σ_{ij} and the actual value of the damage variables D_{ij} . As the stress components σ_{ij} give no indication of reserve to failure, new stress measures have been developed [21]. The *fatigue failure indices* Σ_{ij}^{2D} ($i, j = 1, 2$) for in-plane fatigue loading can be calculated from the Tsai-Wu static failure criterion by replacing the nominal stresses σ_{ij} with the effective stresses $\sigma_{ij}/(1-D_{ij})$. The corresponding fatigue failure index Σ_{11}^{2D} for the stress component σ_{11} is defined as the positive root of the equation [21]:

$$\begin{aligned} & \left(\frac{1}{X_T} - \frac{1}{|X_C|} \right) \frac{\sigma_{11}}{\Sigma_{11}^{2D} \cdot (1-D_{11})} + \left(\frac{1}{Y_T} - \frac{1}{|Y_C|} \right) \frac{\sigma_{22}}{1-D_{22}} + \frac{1}{X_T \cdot |X_C|} \left(\frac{\sigma_{11}}{\Sigma_{11}^{2D} \cdot (1-D_{11})} \right)^2 \\ & + \frac{1}{Y_T \cdot |Y_C|} \left(\frac{\sigma_{22}}{1-D_{22}} \right)^2 + \frac{1}{S^2} \left(\frac{\sigma_{12}}{1-D_{12}} \right)^2 = 1 \end{aligned} \quad (3)$$

The fatigue failure index Σ_{22}^{2D} for the stress component σ_{22} is defined as the positive root of the equation [21]:

$$\begin{aligned} & \left(\frac{1}{X_T} - \frac{1}{|X_C|} \right) \frac{\sigma_{11}}{1-D_{11}} + \left(\frac{1}{Y_T} - \frac{1}{|Y_C|} \right) \frac{\sigma_{22}}{\Sigma_{22}^{2D} \cdot (1-D_{22})} + \frac{1}{X_T \cdot |X_C|} \left(\frac{\sigma_{11}}{1-D_{11}} \right)^2 \\ & + \frac{1}{Y_T \cdot |Y_C|} \left(\frac{\sigma_{22}}{\Sigma_{22}^{2D} \cdot (1-D_{22})} \right)^2 + \frac{1}{S^2} \left(\frac{\sigma_{12}}{1-D_{12}} \right)^2 = 1 \end{aligned} \quad (4)$$

Finally, the fatigue failure index Σ_{12}^{2D} for the stress component σ_{12} is defined as the positive root of the equation [21]:

$$\begin{aligned} & \left(\frac{1}{X_T} - \frac{1}{|X_C|} \right) \frac{\sigma_{11}}{1-D_{11}} + \left(\frac{1}{Y_T} - \frac{1}{|Y_C|} \right) \frac{\sigma_{22}}{1-D_{22}} + \frac{1}{X_T \cdot |X_C|} \left(\frac{\sigma_{11}}{1-D_{11}} \right)^2 \\ & + \frac{1}{Y_T \cdot |Y_C|} \left(\frac{\sigma_{22}}{1-D_{22}} \right)^2 + \frac{1}{S^2} \left(\frac{\sigma_{12}}{\Sigma_{12}^{2D} \cdot (1-D_{12})} \right)^2 = 1 \end{aligned} \quad (5)$$

These *fatigue failure indices* Σ_{11}^{2D} , Σ_{22}^{2D} and Σ_{12}^{2D} quantify the directional reserves to failure in in-plane loading conditions, taking into account the present damage state (D_{11} , D_{22} , D_{12}).

To assess the *relative importance of the separate stress components* σ_{ij} in the failure event, it is better to correlate the failure indices Σ_{ij}^{2D} ($i, j=1,2$) with their one-dimensional equivalent. Also, the failure indices must reduce to their one-dimensional equivalent if the other stress components are zero.

A definition which satisfies these requirements, is the following:

$$\begin{aligned} \Sigma_{11} &= \frac{\Sigma_{11}^{2D}}{1 + (\Sigma_{11}^{2D} - \Sigma_{11}^{1D})} \\ \Sigma_{22} &= \frac{\Sigma_{22}^{2D}}{1 + (\Sigma_{22}^{2D} - \Sigma_{22}^{1D})} \\ \Sigma_{12} &= \frac{\Sigma_{12}^{2D}}{1 + (\Sigma_{12}^{2D} - \Sigma_{12}^{1D})} \end{aligned} \quad (6)$$

The failure indices Σ_{11}^{2D} , Σ_{22}^{2D} and Σ_{12}^{2D} are calculated from the respective equations (3), (4) and (5), while the one-dimensional failure indices Σ_{11}^{1D} , Σ_{22}^{1D} and Σ_{12}^{1D} are defined as the ratio of the effective stress $\tilde{\sigma}$ to the respective static strength. So, the two-dimensional failure

indices Σ_{ij}^{2D} ($i, j = 1, 2$) take into account the effect of multi-axial loading, while the correlation with the one-dimensional ratio Σ_{ij}^{1D} ($i, j = 1, 2$) to their respective static strengths indicates the relative probability of failure along the considered direction \vec{e}_{11} or \vec{e}_{22} . The newly defined failure indices reduce to their one-dimensional equivalent if a one-dimensional stress is applied, so the relation between one-dimensional and multi-dimensional failure indices remains consistent in use. As the Tsai-Wu failure criterion itself is not based on physical grounds (damage modes, micromechanical observations,...), but on a quadratic tensorial formulation, the physical background of Equation (6) is limited to the fact that dimensionless fatigue failure indices Σ_{ij} ($i, j = 1, 2$) have been derived from the Tsai-Wu failure criterion and that these stress-based parameters affect the growth rate of the directional damage variables D_{ij} ($i, j = 1, 2$). For this material, these failure indices Σ_{ij} ($i, j = 1, 2$) have proven to be reliable measures of the stress state ($\sigma_{11}, \sigma_{22}, \sigma_{12}$) in the presence of damage.

It is important to observe that if the stress state approaches the Tsai-Wu failure surface, not all failure indices Σ_{ij} ($i, j = 1, 2$) will reach the failure value 1.0, because the failure indices are normalized with respect to their one-dimensional ratio Σ_{ij}^{1D} ($i, j = 1, 2$). To avoid any singularities in the equations (3), (4) and (5) during fatigue life simulation, the calculation strategy is as follows:

- if one of the failure indices Σ_{ij} ($i, j = 1, 2$) has a high value, the corresponding damage variable D_{ij} will grow very rapidly,
- if this failure index Σ_{ij} approaches its failure value 1.0, the corresponding stress σ_{ij} is set to zero,
- in the next evaluation of the Tsai-Wu failure indices, all terms in the stress component σ_{ij} are zero.

A detailed discussion of the damage-dependent directional failure indices Σ_{ij} can be found in [21].

In the end the close feedback between experimental observations and finite element predictions has lead to the final damage growth rate equations for generalized in-plane fatigue loading [20]:

$$\begin{aligned}
 \frac{dD_{11}}{dN} &= \begin{cases} c_1 \cdot (1 + D_{12}^2) \cdot \Sigma_{11} \cdot \exp\left(-c_2 \frac{D_{11}}{\sqrt{\Sigma_{11}} \cdot (1 + D_{12}^2)}\right) & \text{if } \sigma_{11} \geq 0 \\ + c_3 \cdot D_{11} \cdot \Sigma_{11}^2 \cdot [1 + \exp(c_5(\Sigma_{11} - c_4))] & \end{cases} \\
 \frac{dD_{11}}{dN} &= \begin{cases} \left[c_1 \cdot (1 + D_{12}^2) \cdot \Sigma_{11} \cdot \exp\left(-c_2 \frac{D_{11}}{\sqrt{\Sigma_{11}} \cdot (1 + D_{12}^2)}\right) \right]^{1+2 \cdot \exp(-D_{12})} & \text{if } \sigma_{11} < 0 \\ + c_3 \cdot D_{11} \cdot \Sigma_{11}^2 \cdot \left[1 + \exp\left(\frac{c_5}{3}(\Sigma_{11} - c_4)\right) \right] & \end{cases} \\
 \\
 \frac{dD_{22}}{dN} &= \begin{cases} c_1 \cdot (1 + D_{12}^2) \cdot \Sigma_{22} \cdot \exp\left(-c_2 \frac{D_{22}}{\sqrt{\Sigma_{22}} \cdot (1 + D_{12}^2)}\right) & \text{if } \sigma_{22} \geq 0 \\ + c_3 \cdot D_{22} \cdot \Sigma_{22}^2 \cdot [1 + \exp(c_5(\Sigma_{22} - c_4))] & \end{cases} \\
 \frac{dD_{22}}{dN} &= \begin{cases} \left[c_1 \cdot (1 + D_{12}^2) \cdot \Sigma_{22} \cdot \exp\left(-c_2 \frac{D_{22}}{\sqrt{\Sigma_{22}} \cdot (1 + D_{12}^2)}\right) \right]^{1+2 \cdot \exp(-D_{12})} & \text{if } \sigma_{22} < 0 \\ + c_3 \cdot D_{22} \cdot \Sigma_{22}^2 \cdot \left[1 + \exp\left(\frac{c_5}{3}(\Sigma_{22} - c_4)\right) \right] & \end{cases} \\
 \\
 \frac{dD_{12}}{dN} &= c_1 \cdot \Sigma_{12} \cdot \exp\left(-c_2 \frac{D_{12}}{2\sqrt{\Sigma_{12}}}\right) \tag{7}
 \end{aligned}$$

4.2.3 Growth Laws for Permanent Strains

Finally, additional equations for the growth rate of the permanent strains ε_{ii}^p ($i = 1,2$) must be established. The permanent deformation is considerable (see Figure 5 and 6), and cannot be denied in this particular case. The problem however, is that there is almost no literature available on how this permanent deformation should be modelled, let alone under fatigue. Although the adequate modelling of this permanent strain phenomenon would require a research project on its own, an attempt is made to give at least an impression of the importance of this phenomenon in the particular loading case considered here.

The proposed fatigue damage evolution law for the permanent strain is based on a rational modelling of the underlying damage kinetics, and a few assumptions might be legitimate:

- the permanent strain is related with the shear damage D_{12} , since the phenomenon is hardly observed with the $[\#0^\circ]_8$ specimens. Besides, the explanation is very plausible that matrix debris, formed by the shear stresses, is accumulated in the opening matrix cracks. It can therefore be assumed that the growth rate of the permanent strain is proportional with the growth rate of the shear damage D_{12} ,
- the more the matrix cracks open during fatigue loading, the more matrix debris can be accumulated inside the crack opening. The permanent strain growth rate in the \vec{e}_{11} and \vec{e}_{22}

direction might therefore be proportional with the applied strain amplitude in the respective directions \vec{e}_{11} and \vec{e}_{22} ,

- as the cracks do not open at the compressive side, it is further accepted that the permanent strain does not grow if the applied stress is compressive.

The corresponding growth laws for the permanent strain have been written as (no summation convention) [20]:

$$\frac{d\varepsilon_{ii}^p}{dN} = \begin{cases} c_6 \cdot \varepsilon_{ii} \cdot \frac{dD_{12}}{dN} & \text{if } \sigma_{ii} \geq 0 \\ 0 & \text{if } \sigma_{ii} < 0 \end{cases} \quad (i = 1, 2) \quad (8)$$

The factor c_6 has been determined such that the predicted out-of-plane displacement profile after unloading matches the experimentally recorded one for the $[\#45^\circ]_8$ specimen Pr06_1. This was the case for $c_6 = 0.6$. This implies that, if the damage D_{12} reaches its failure value 1.0, the permanent strain ε_{ii}^p cannot be larger than 60 % of the total strain amplitude ε_{ii} .

The growth laws for the permanent strains remain valid for the $[\#0^\circ]_8$ stacking sequence too. Loading of this specimens would not result in any shear strains. As a result, the growth rate of shear damage D_{12} would be zero and the permanent strains ε_{11}^p and ε_{22}^p would remain zero. That is in agreement with the experimental findings, where the $[\#0^\circ]_8$ specimens showed no permanent deformation (unless after complete failure, when fibres where broken at the clamped cross-section).

5 Finite Element Implementation

All constitutive equations have been implemented in the commercial finite element code SAMCEFTM. The composite specimen has been modelled with isoparametric solid brick elements, one element through the thickness for each of the eight composite plies (see Figure 7).

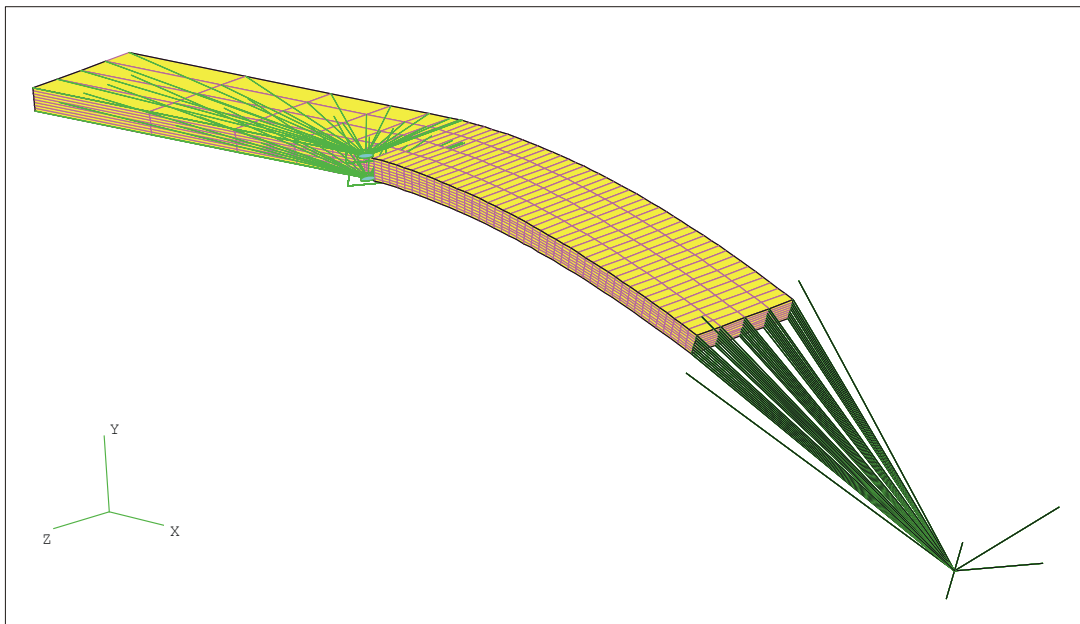


Figure 7: Finite element model of the bending fatigue setup.

Further the clamping plates at the fixation and the displacement mechanism at the lower specimen end have been included in the finite element mesh. It has been shown that the correct modelling of the boundary conditions is extremely important to yield reliable results.

The whole fatigue life from the first loading cycle up till final failure is simulated, and stiffness degradation, stress redistribution, and accumulation of permanent strain are accounted for. As it is impossible to simulate each individual fatigue loading cycle, an adaptive time stepping algorithm has been implemented. The algorithm evaluates how many cycles can be jumped over without losing accuracy on the evolution and growth of damage in all integration points of the finite element mesh. It is assumed that the damage increments $d(D_{ij})/dN$ are constant during these *cycle jumps*. The *cycle jump* concept is schematically illustrated in Figure 8.

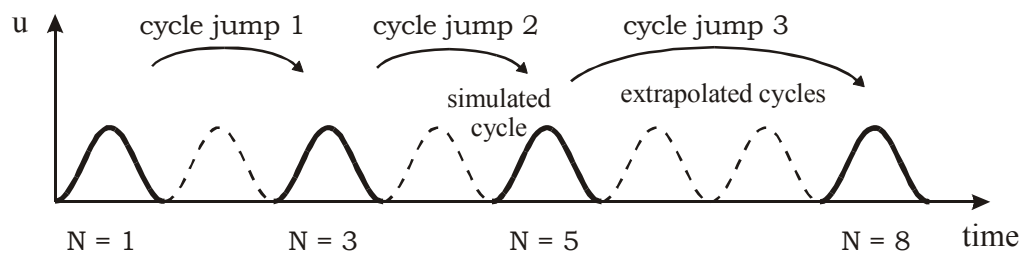


Figure 8: Schematic illustration of the *cycle jump* concept [22].

It is clear that the evaluation of the *cycle jump* size is the possible Achilles heel of the concept: when the *cycle jump* size is determined very conservatively, the simulation will be rather accurate, because the differential equations are integrated with very small increments of the cycle number N . However, the computational effort will be huge, because almost every single cycle would be simulated. On the other hand, when the *cycle jump* N_{JUMP} is too large, the predicted damage values for the next loading cycle $N+N_{JUMP}$ will be rather different from the exact solution of the differential equation.

Further it is important to note that there is no communication with the post-processing module during the complete finite element simulation of the fatigue tests: the *cycle jumps* are performed in the core of the finite element analysis module, and control is only returned to the post-processing environment when the full number of cycles has been simulated. This implies that there is no feedback-procedure possible to compare at any cycle the predicted force-cycle history with the experimentally measured force-cycle history, and to make an evaluation of the *cycle jump* size. Of course such a feedback-procedure cannot be intended either, since the ultimate goal of an intrinsic material damage model is to simulate the material's behaviour under certain loading conditions without any foreknowledge of the experimental results. Even from the numerical point of view such a feedback-procedure is not desirable because it would significantly increase the computational effort. Each time that the *cycle jump* would appear to be too large, the calculation should be restored at the previous time step and the previous damage state should be reloaded.

Finally, the fatigue damage model should be intrinsic to the material used and should be local in nature, because the SAMCEFTM user interface loops over all Gauss-points and there is no information transfer from one Gauss-point to another. For each Gauss-point, the stress-, strain- and stiffness-tensor are available, and only after that the damage for that particular Gauss-point is evaluated, the procedure switches to the following Gauss-point.

The *cycle jump* NJUMP is determined in two stages: (i) first, the local *cycle jump* NJUMP1 is calculated separately for each Gauss-point, based on the local stress and damage state in the Gauss-point itself, and next (ii), the global *cycle jump* NJUMP is calculated from all local *cycle jump* values NJUMP1.

Now it is matter of defining the criterion for calculating these local NJUMP1 values, and from these values, the global *cycle jump* NJUMP.

5.1. Determination of the local *cycle jump* NJUMP1

The damage values have been chosen to determine the local *cycle jumps* due to their favourable properties compared to the stress values: their value is always lying between 0 and 1 and monotonically increasing. One possible and straightforward method to tackle the problem of calculating the local *cycle jump* NJUMP1 is to use the simple Euler explicit integration formula for evaluating the local increase of the damage variables for each Gauss-point:

$$\text{NJUMP1} = \text{minimum} \left(\frac{D_{ij,N+\text{NJUMP1}} - D_{ij,N}}{\left. \frac{dD_{ij}}{dN} \right|_N} \right) = \frac{\Delta D_{ij}}{\left. \frac{dD_{ij}}{dN} \right|_N} \quad (9)$$

Based on the same philosophy, more accurate numerical techniques can be applied. For example, the damage variables D_{ij} could be numerically extrapolated to $D_{ij} + \Delta D_{ij}$, taking into account the full damage-cycle history information, instead of using only the last known damage value with the Euler method. However this does not limit the applicability of the approach presented here.

The value of the maximum allowed increase ΔD_{ij} should not be set in *absolute terms*. If the maximum allowed increase of damage was set to be for example 0.1, heavily loaded integration points could reach that increase in a few hundred cycles, while it could take integration points loaded at a very low stress level, several thousands of cycles to reach that absolute increment of 0.1. Therefore it is more appropriate to define the increase in *relative terms* to the present value of the damage for small values of D_{ij} . The used criterion was:

$$\Delta D_{ij} = \begin{cases} 10^{-9} & \text{if } D_{ij} = 0 \\ 0.5 \cdot D_{ij} & \text{if } 0 < D_{ij} \leq 0.2 \\ 0.1 & \text{if } D_{ij} > 0.2 \end{cases} \quad (10)$$

5.2. Determination of the global *cycle jump* NJUMP

The simplest approach is to define NJUMP as the minimum value of all NJUMP1 values, but this is not recommended, because normally at each moment in the fatigue life of the composite construction, there are Gauss-points with fast increasing damage variables D_{ij} . Hence the NJUMP1 value will be small. As a consequence, the global *cycle jump* NJUMP will always be small and the calculation will proceed too slowly.

Therefore it is assumed that the global *cycle jump* NJUMP can best be taken as a small percentile of the cumulative relative frequency distribution of all NJUMP1 values. A small percentage of the Gauss-points will be imposed a larger *cycle jump* than the NJUMP1 value that was considered to be safe for these Gauss-points. However these Gauss-points will just be the ones that are already seriously damaged and where extrapolation errors will be rather negligible.

Figure 9 shows an example of the relative frequency distribution for the finite element calculation of a standard bending fatigue experiment, whereby it is assumed that the maximum allowed value of the local *cycle jump* NJUMP1 is 100000 cycles.

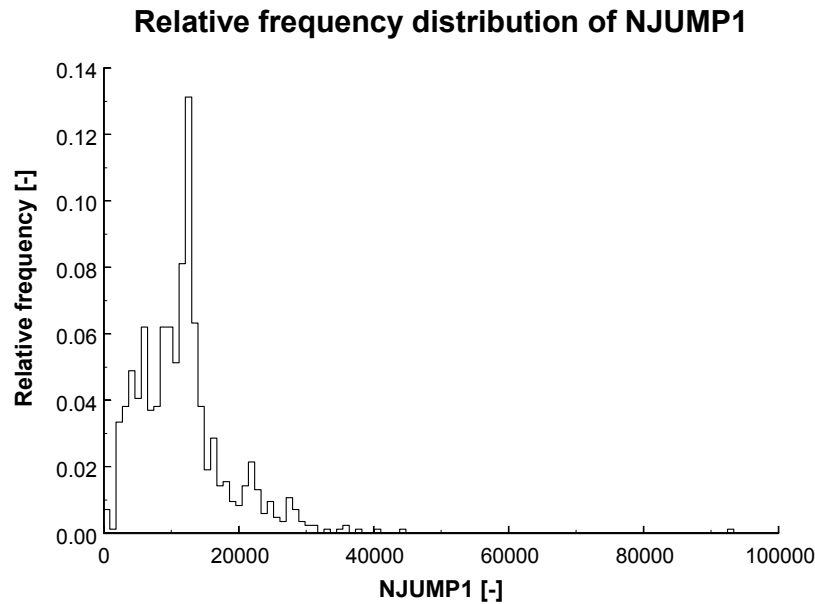


Figure 9: Relative frequency distribution of NJUMP1.

To determine the relative frequency distribution, the range of 100000 cycles in Figure 9 is divided into a number of intervals, called ‘classes’ in the statistics terminology. Then it is counted how many NJUMP1 values are lying in a particular class. This number, divided by the total number of NJUMP1 values, is the relative frequency of that particular class.

In this particular example, there are 838 Gauss-points and the number of classes of the frequency distribution is 100. It is worth to notice that there are a small number of Gauss-points in the class 92000 to 93000; for these Gauss-points a very large *cycle jump* seems safe, although for the vast majority of the Gauss-points the *cycle jump* stays below 20000 cycles.

Next Figure 10 shows the cumulative relative frequency distribution. When for example the 10 % percentile of the cumulative relative frequency distribution is considered, the value of the global *cycle jump* NJUMP would be 4078 cycles.

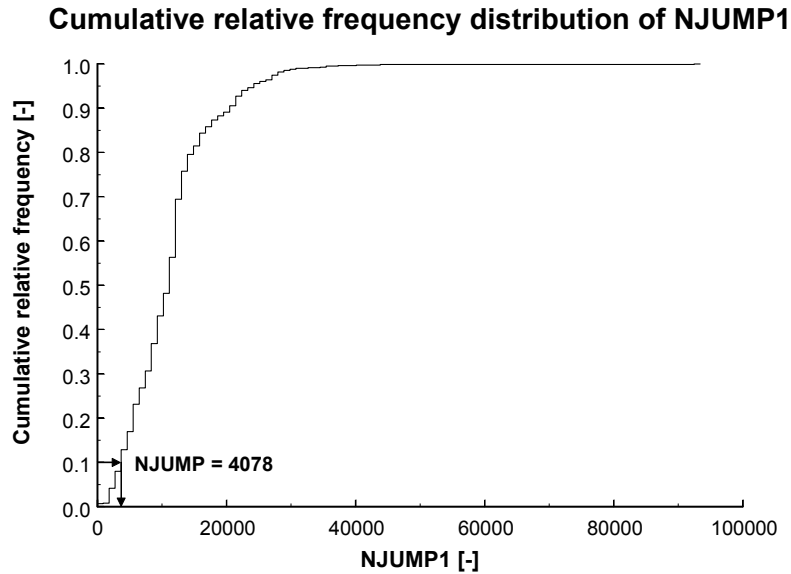


Figure 10: Cumulative relative frequency distribution of NJUMP1.

6 Example of Finite Element Simulation

The finite element simulation concerns the bending fatigue test Pr06_3, which was performed for $u_{\max} = 38.9$ mm. As can be seen from Figure 11, the initial force degradation is really large, about 25 Newton.

Experimental and simulated force-cycle history for $[\#45^\circ]_8$ specimen single-sided bending, $u_{\max} = 38.9$ mm

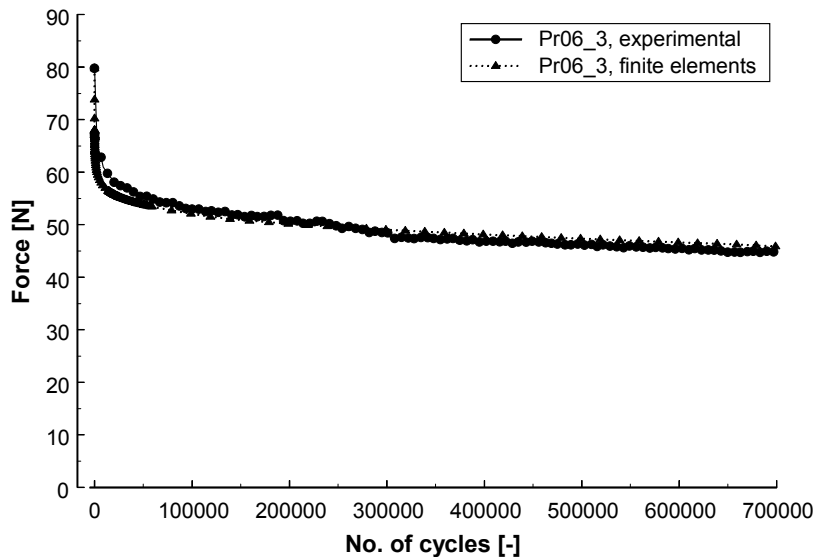


Figure 11: Experimental and simulated force-cycle history for the $[\#45^\circ]_8$ specimen Pr06_3 ($u_{\max} = 38.9$ mm).

Also, the permanent deformation is considerable, due to the large prescribed displacement. Figure 12 shows the experimental and simulated permanent deformation after 700000 cycles for the Pr06_3 specimen.

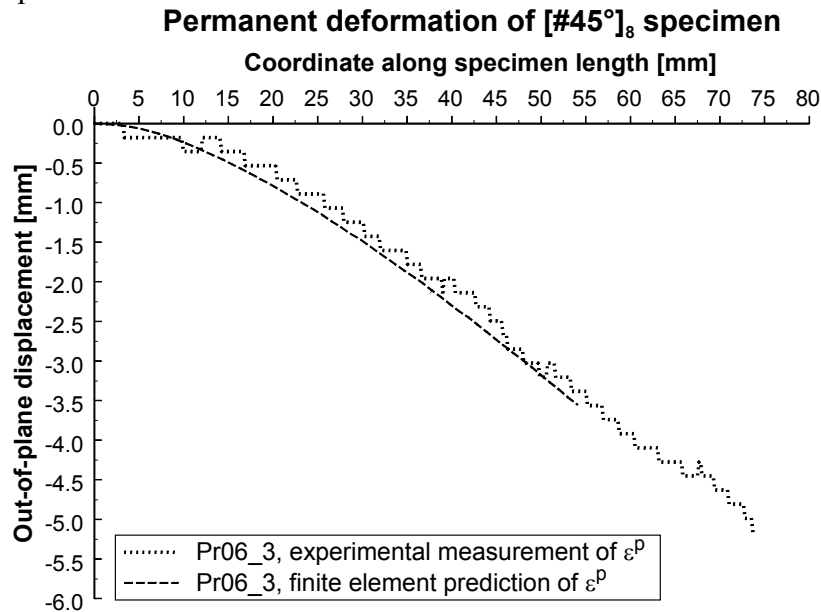


Figure 12: Experimental and predicted permanent deformation of [#45°]₈ specimen Pr06_3 after 700000 cycles.

Figure 13 shows the simulated distribution of the stress σ_{11} at the clamped cross-section at several stages during fatigue life. The accumulation of permanent strain at the tensile side causes the initial stresses to decrease much more than the stresses at the compressive side of the specimen.

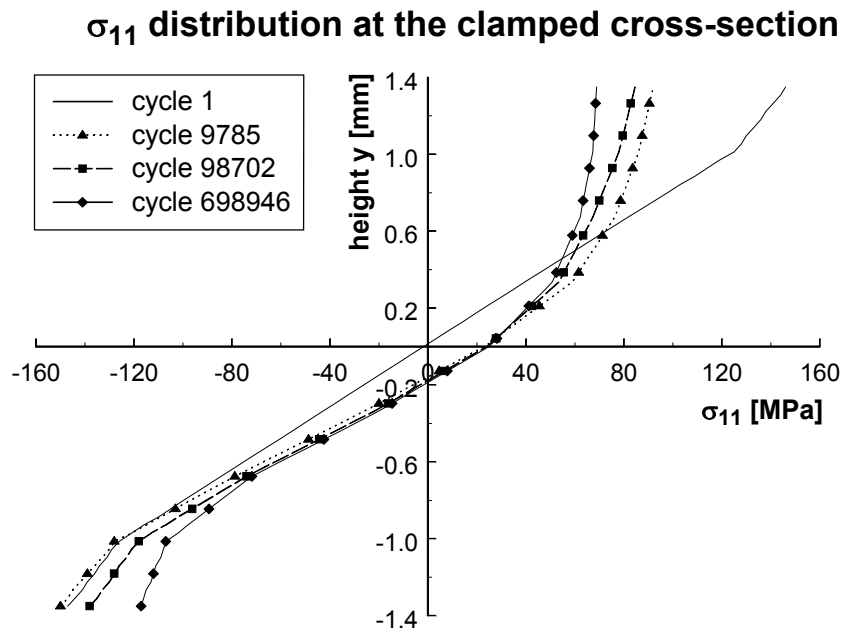


Figure 13: Simulated distribution of σ_{11} at the clamped cross-section for the $[\#45^\circ]_8$ specimen Pr06_3 ($u_{\max} = 38.9$ mm).

It is obvious that the distribution of the stress σ_{22} is the same, since the principal material axes \vec{e}_{11} and \vec{e}_{22} of the $[\#45^\circ]_8$ specimens are situated symmetrically with respect to the loading direction.

7 Conclusion

From experimental observations, it was concluded that fatigue damage can give rise to several phenomena in fibre-reinforced plastics: (gradual) stiffness degradation, varying displacement profile in bending, accumulation of permanent strain.

If one is interested in the growth of these phenomena, and not only in the moment of failure (i.e. the number of cycles to failure), then a damage model must be established. The fatigue damage model in this paper was based on a continuum damage mechanics approach, where selected damage variables are representing the stiffness degradation and their effect on the elastic properties. Combined with a modified interpretation of the Tsai-Wu failure criterion, the model is able to simulate the fatigue behaviour from the first loading cycle up to final failure.

References

- [1] J. Degrieck, W. Van Paepegem, “*Fatigue Damage Modelling of Fibre-Reinforced Composite Materials: Review*”, *Applied Mechanics Reviews*, 54(4), 279-300, 2001.
- [2] C.M. Lawrence Wu, “*Thermal and mechanical fatigue analysis of CFRP laminates*”, *Composite Structures*, 25, 339-344, 1993.
- [3] M.-H.R. Jen, C.-H. Lee, “*Strength and life in thermoplastic composite laminates under static and fatigue loads. Part I: Experimental*”, *International Journal of Fatigue*, 20(9), 605-615, 1998.
- [4] M.-H.R. Jen, C.-H. Lee, “*Strength and life in thermoplastic composite laminates under static and fatigue loads. Part II: Formulation*”, *International Journal of Fatigue*, 20(9), 617-629, 1998.
- [5] T.P. Philippidis, A.P. Vassilopoulos, “*Fatigue strength prediction under multiaxial stress*”, *Journal of Composite Materials*, 33(17), 1578-1599, 1999.
- [6] R. Talreja, “*Stiffness properties of composite laminates with matrix cracking and interior delamination*”, *Engineering Fracture Mechanics*, 25(5/6), 751-762, 1986.
- [7] R. Talreja, “*Damage mechanics of composite materials based on thermodynamics with internal variables*”, *Durability of polymer based composite systems for structural applications. Proceedings of the International Colloquium, 27-31 August 1990, Brussels, Belgium, Elsevier*, pp. 65-79, 1990.
- [8] D.H. Allen, C.E. Harris, S.E. Groves, “*A thermomechanical constitutive theory for elastic composites with distributed damage - I. Theoretical development*”, *International Journal of Solids and Structures*, 23(9), 1301-1318, 1987.
- [9] D.H. Allen, C.E. Harris, S.E. Groves, “*A thermomechanical constitutive*

- theory for elastic composites with distributed damage - II. Application to matrix cracking in laminated composites*", *International Journal of Solids & Structures*, 23(9), 1319-1338, 1987
- [10] A. Sedrakian, T. Ben Zineb, J.L. Billoet, N. Sicot, P. Lardeur, "A numerical model of fatigue behaviour for composite plates: application to a three point bending test", *International Conference on fatigue of composites. Proceedings*, 3-5 June 1997, Paris, France, La Société Française de Métallurgie et de Matériaux, pp. 415-423, 1997.
- [11] A. Sedrakian, T. Ben Zineb, J.L. Billoet, V. Bobet, "Fatigue behaviour simulation of industrial composite parts", *Proceedings of the Second International Conference on Fatigue of Composites*. 4-7 June 2000, Williamsburg, pp. 4.5-4.6, 2000.
- [12] M.M. Shokrieh, L.B. Lessard, "Multiaxial fatigue behaviour of unidirectional plies based on uniaxial fatigue experiments - I. Modelling", *International Journal of Fatigue*, 19(3), 201-207, 1997.
- [13] M.M. Shokrieh, L.B. Lessard, "Multiaxial fatigue behaviour of unidirectional plies based on uniaxial fatigue experiments - II. Experimental evaluation", *International Journal of Fatigue*, 19(3), 209-217, 1997.
- [14] G. Lubin, S.J. Dastin, "Aerospace applications of composites", *Handbook of Composites*. New York, Van Nostrand Reinhold Company Inc., pp. 722-743, 1992.
- [15] J.A. Bailie, "Woven fabric aerospace structures", *Handbook of Composites*. Volume 2 : Structures and design. Amsterdam, Elsevier, pp. 353-391, 1989.
- [16] J. Degrieck, W. Van Paepegem, P. Boone, "Application of digital phase-shift shadow Moiré to micro deformation measurements of curved surfaces", *Optics and Lasers in Engineering*, 36, 29-40, 2001.
- [17] W. Van Paepegem, J. Degrieck (2002), "Coupled Residual Stiffness and Strength Model for Fatigue of Fibre-reinforced Composite Materials", *Composites Science and Technology*, 62(5), 687-696.
- [18] W. Van Paepegem, J. Degrieck (2002), "A New Coupled Approach of Residual Stiffness and Strength for Fatigue of Fibre-reinforced Composites", *International Journal of Fatigue*, 24(7), 747-762.
- [19] W. Van Paepegem, J. Degrieck (2002), "Tensile and Compressive Damage Coupling for Fully-reversed Bending Fatigue of Fibre-reinforced Composites", *Fatigue and Fracture of Engineering Materials & Structures*, 25(6), 547-562.
- [20] W. Van Paepegem, "Development and finite element implementation of a damage model for fatigue of fibre-reinforced polymers", Ph.D. thesis. Gent, Belgium, Ghent University Architectural and Engineering Press (ISBN 90-76714-13-4), 403 p., 2002.
- [21] W. Van Paepegem, J. Degrieck, "Calculation of Damage-dependent Directional Failure Indices from the Tsai-Wu Static Failure Criterion", *Composites Science and Technology*, 63(2), 305-310, 2002.
- [22] W. Van Paepegem, J. Degrieck, P. De Baets (2001), "Finite Element Approach for Modelling Fatigue Damage in Fibre-reinforced Composite Materials", *Composites Part B*, 32(7), 575-588.